



Structural, electrical and dielectric studies on $(1-x)\text{MgTiO}_3-x\text{Ba}_{0.5}\text{Sr}_{0.5}\text{TiO}_3$ composite ceramics for type-II capacitor applications

Susmita Rabha¹ · Pamu Dobbidi¹

Received: 15 October 2018 / Accepted: 1 February 2019 / Published online: 13 March 2019
© Springer Science+Business Media, LLC, part of Springer Nature 2019

Abstract

The structural, microstructural, electrical and broadband dielectric properties of $(1-x)\text{MgTiO}_3-x\text{Ba}_{0.5}\text{Sr}_{0.5}\text{TiO}_3$ (for $x=0.1$ to 0.5) composite ceramics has been reported. Conventional solid state reaction method is followed for preparation of the powder and maximum densification is optimized at different sintering temperatures (1250 to 1400 °C). The structural studies revealed presence of both MTO and BST phases independently. The cryogenic dielectric response was studied over a broadband frequency range. The composite ceramics have exhibited diffused transition as a typical signature of relaxor ferroelectrics with temperature. Modified Curie–Weiss law is implemented and calculated the diffuseness constant to probe the relaxor behavior of the ceramics. The Impedance analysis in complex plane showed non-Debye type relaxation behavior. Correlated barrier hopping mechanism is found to be responsible for conduction process at higher frequency region in AC-conductivity analysis. The thermal stability of capacitance over the temperature range of (RT) – 30 to + 85 °C determined and found to be ~ – 54%. The 0.7 MTO—0.3 BST ceramic composite sintered at a temperature (T_s) of 1350 °C is optimized as the best composition with the highest values of relative density (~ 97%), high dielectric permittivity $\epsilon_r \sim 57$ and quality factor, $Q \times f_0 = 19,30$ GHz at 4.16 GHz. The obtained properties of the composite ceramics is promising for type -II capacitors in integrated circuits of de-couplers and filters.

The rapid growth in telecommunication technology has lead to an increasing demand for microwave ceramics and thin films. Various ceramic materials were developed and studied based on its electrical storage capacity (C). Apart from the materials for electrical storage device, materials for tunable microwave device are also in great demand [1]. In telecommunication industry, electric field tunable ferroelectric ceramics were widely studied for applications in phase shifters, tunable dielectric filters, delay lines and other microwave devices [2]. In addition, solid solution of linear dielectric and ferroelectric ceramics with comparatively lower dielectric permittivity and loss tangent have also been studied for their potential application in tunable microwave devices [3]. Studies have shown that materials with high permittivity, ϵ_r ($30 < \epsilon_r < 1500$) and low loss ($\tan\delta < 0.01$) are required for the high performance compact integrated circuit (IC) applications [2]. Further, the ceramic capacitors were categorized into two types as type-I and type-II capacitor

based on their dielectric constant and thermal stability over a range of operating temperature. For type-I capacitor, moderate dielectric constant, low loss tangent and high thermal stability is required and are used in resonant circuit applications. Whereas, the type-II capacitors need high dielectric constant, which enables miniaturization of the device size and are promising for de-couplers and filters [4]. Generally, type-II capacitors exhibit non-linear temperature co-efficient and exhibits capacitance that is dependent on small degree of applied voltage. Further, type-II capacitors were classified based on the value of temperature co-efficient of capacitance and operating temperature range. Among them X7R and Z5U are popular type-II capacitors. X7R have temperature co-efficient of capacitance < 15% in operating temperature of – 55 to 125 °C, whereas Z5U should have temperature co-efficient of capacitance in the range of 22 to – 85% in the operating temperature range of – 30 to 85 °C [5].

MgTiO_3 , a linear dielectric ceramic has been widely investigated due to its excellent properties at microwave frequencies: extremely low loss ($\tan\delta \sim 10^{-4}$), moderate dielectric permittivity ($\epsilon_r \approx 17$) and thermal stability ($\tau_f \approx -50$ ppm/°C) [6]. On the other hand, $\text{Ba}_{0.5}\text{Sr}_{0.5}\text{TiO}_3$, a ferroelectric ceramic exhibits high dielectric permittivity,

✉ Pamu Dobbidi
pamu@iitg.ac.in

¹ Indian Institute of Technology Guwahati, Guwahati, Assam 781039, India

low loss and tunable dielectric permittivity with DC (Direct current) biasing [2, 7]. There are various reports on Mg doped $\text{Ba}_{0.5}\text{Sr}_{0.5}\text{TiO}_3$ to reduce its dielectric loss and permittivity for considering applications in tunable phase shifter, filters antenna etc., [8]. Su et al. [9], reported the effect of Mg doping on the dielectric and microstructural properties of $\text{Ba}_{0.8}\text{Sr}_{0.2}\text{TiO}_3$ ceramics and maximum solubility limit of Mg have been reported as 2 wt%. Shanming Ke et al. [10], had reported the effect of MgTiO_3 on $\text{Ba}_{0.6}\text{Sr}_{0.4}\text{TiO}_3$ ceramics and achieved a significant reduction in the dielectric loss (0.003) for 8 mol% addition of MgTiO_3 . However, there is no systematic study available on BST added MgTiO_3 ceramic system and their microwave dielectric, electrical properties and impedance analysis etc. Impedance spectroscopy is a viable tool to understand physical properties of such systems. With the help of impedance spectroscopy, electrical response corresponding to various electrically active regions can be realized qualitatively from electrical responses and quantitatively from impedance analysis [11].

The literature till date, have mainly focused on doping of Mg based ceramics into BST to reduce the dielectric loss. In the present study, BST has been added to MTO ceramics and the effect of BST on the structural, microstructural and dielectric properties of MTO ceramics have been studied systematically as a function of sintering temperature. The broadband (1 MHz to 1 GHz) dielectric response also been reported in this study for the first time. Further, in the present study, it is proposed that the addition of BST in MTO ceramics will definitely enhance the storage capacity (dielectric constant) and dielectric loss. Proper optimization in composition is essential to enhance the dielectric constant with least effect on the Q value of MgTiO_3 ceramics for microwave tunable applications. Further, the best optimized composite sample was chosen to study the impedance spectra at different temperatures to understand the relation between the dielectric response and microstructure.

1 Materials and methods

The composite ceramics were prepared by solid state reaction method using MgTiO_3 (MTO) and $\text{Ba}_{0.5}\text{Sr}_{0.5}\text{TiO}_3$ (BST) ceramic powders. Initially, the MgTiO_3 (MTO) ceramic powder was prepared by using highly pure powders of MgO (99.99%) and TiO_2 (99.99%) from M/s Sigma Aldrich, USA. To avoid secondary phase formation of MTO at higher sintering temperature, non-stoichiometric composition of MgTiO_3 ($\text{Mg}_{(1+0.07)}\text{TiO}_3$) was used [6]. Similarly, $\text{Ba}_{0.5}\text{Sr}_{0.5}\text{TiO}_3$ (BST) ceramic powder was also prepared by using high purity powders of BaCO_3 (99.99%), SrCO_3 (99.99%) and TiO_2 (99.99%) from M/s Sigma Aldrich, USA. The powders were first weighed in appropriate proportions and ball milled in the liquid medium of distilled water for 5 h

using a planetary ball mill (Pulversitte 6, M/s Fritsch GmbH, Germany). The obtained slurry was then dried at 150 °C and the powders obtained were calcined at 1100 °C for 3 h. Further, for the preparation of $(1-x)\text{MgTiO}_3 - x\text{Ba}_{0.5}\text{Sr}_{0.5}\text{TiO}_3$ ($x = 0.1, 0.2, 0.3, 0.4, 0.5$) composites, the calcined MgTiO_3 and $\text{Ba}_{0.5}\text{Sr}_{0.5}\text{TiO}_3$ powders were ball milled for 5 h according to their composition. The as obtained powders were then pressed into cylindrical discs of diameter 10 mm and thickness ranging from 1 to 5 mm using poly vinyl alcohol as a binder. The pressed discs were finally sintered at 1250 °C, 1300 °C, 1350 °C and 1400 °C for 4 h in air. The prepared composite ceramics have been named accordingly and tabulated in Table 1.

The structural characterizations were carried out by using X-Ray diffractometer (XRD) (TTRAX III 18 KW, M/s Rigaku) employing Cu-K_α radiation ($\lambda = 1.5406 \text{ \AA}$) for crystal structure determination and Raman Spectrometer (Lab RamHR, M/s Horiba JobinYvon) equipped with a He-Ne laser of wavelength 514 nm to study the vibrational modes associated with the composite ceramics. The Archimedes method has been adopted to measure the density of the samples and the values obtained were compared with the theoretical density obtained from the following relation

$$\rho = \frac{\frac{w_1}{\rho_1} + \frac{w_2}{\rho_2}}{\frac{w_1}{\rho_1} + \frac{w_2}{\rho_2}} \quad (1)$$

where w_1 , ρ_1 and w_2 , ρ_2 are the molecular weight fraction and theoretical density obtained from Rietveld refinement of MTO and BST ceramics, respectively. The microstructure and surface morphology were studied by using Field emission scanning electron microscope (FESEM) (JSM-7610F, M/s JEOL) and energy dispersive spectroscopy (EDS) (Sigma, M/s Zeiss) is used for elemental composition analysis. The frequency (100 Hz to 1 MHz) and temperature (30 to 400 °C) dependent dielectric properties were studied using by LCR meter (M/s Wayne Kerr Pvt. Ltd., 4300). Again, temperature dependent the broadband dielectric properties of the ceramics have been studied by using RF impedance analyzer (4991A, M/s Agilent Technologies,) equipped with temperature attachments (BDS 2300, M/s Novocontrol, GmbH, Germany). Microwave dielectric parameters were studied using the vector network analyser (ZVA232, M/s

Table 1 Sample name corresponding to different values of x

x	Sample name
0.1	MTBS1
0.2	MTBS2
0.3	MTBS3
0.4	MTBS4
0.5	MTBS5

Rohde & Schwarz) using Hakki-Coleman method [12, 13]. The loaded quality factor (Q_l) is evaluated by using the expression [14],

$$Q_l = \frac{f_0}{\Delta f} \quad (2)$$

where f_0 and Δf_0 is the resonant frequency and band width at 3 dB down from maximum S_{21} value corresponding to TE_{016} mode. If S_{21} at resonance is less than 45 dB, unloaded Q_u is calculated by using the relation,

$$Q_u = \frac{Q_l}{(1 - \beta_c)} \quad (3)$$

where β_c is coupling coefficient and can be define as, $10^{-\frac{S_{21}}{20}}$. Further, by using iterative Rayleigh–Ritz's method for the calculation of dielectric constant. Accuracy in the measurement is,

$$\frac{\Delta \epsilon}{\epsilon} = T \cdot \frac{\Delta h}{h} + (2 - t) \frac{\Delta d}{d} \text{ for } 0 < T < 2 \quad (4)$$

where, h is the diameter and d is the height of the sample.

$$\Delta \tan \delta = \pm 2.0 \times 10^6 \text{ or } \pm 0.03 \tan \delta \quad (5)$$

2 Results and discussions

2.1 XRD analysis

XRD spectra of the BST-MTO based composite ceramics, sintered at different temperatures (1250–1400 °C) are shown in Fig. 1a–d. The XRD analysis revealed the presence of individual phases of polycrystalline MTO (JCPDS # 790831) of space group $R\bar{3}$ with rhombohedral crystal structure and BST (JCPDS no # 00-0390-1395) of space group $Pm-3m$ with cubic crystal structure. Apart from MTO and BST, peaks corresponding to a mixed phase of MTO-BST # $BaMg_6Ti_6O_{19}$ were also observed and indexed according to JCPDS no #42–441. The sintering temperature have found to be strongly affected the intensities of the corresponding peaks. For a sintering temperature (T_s) 1250 °C, MTBS1

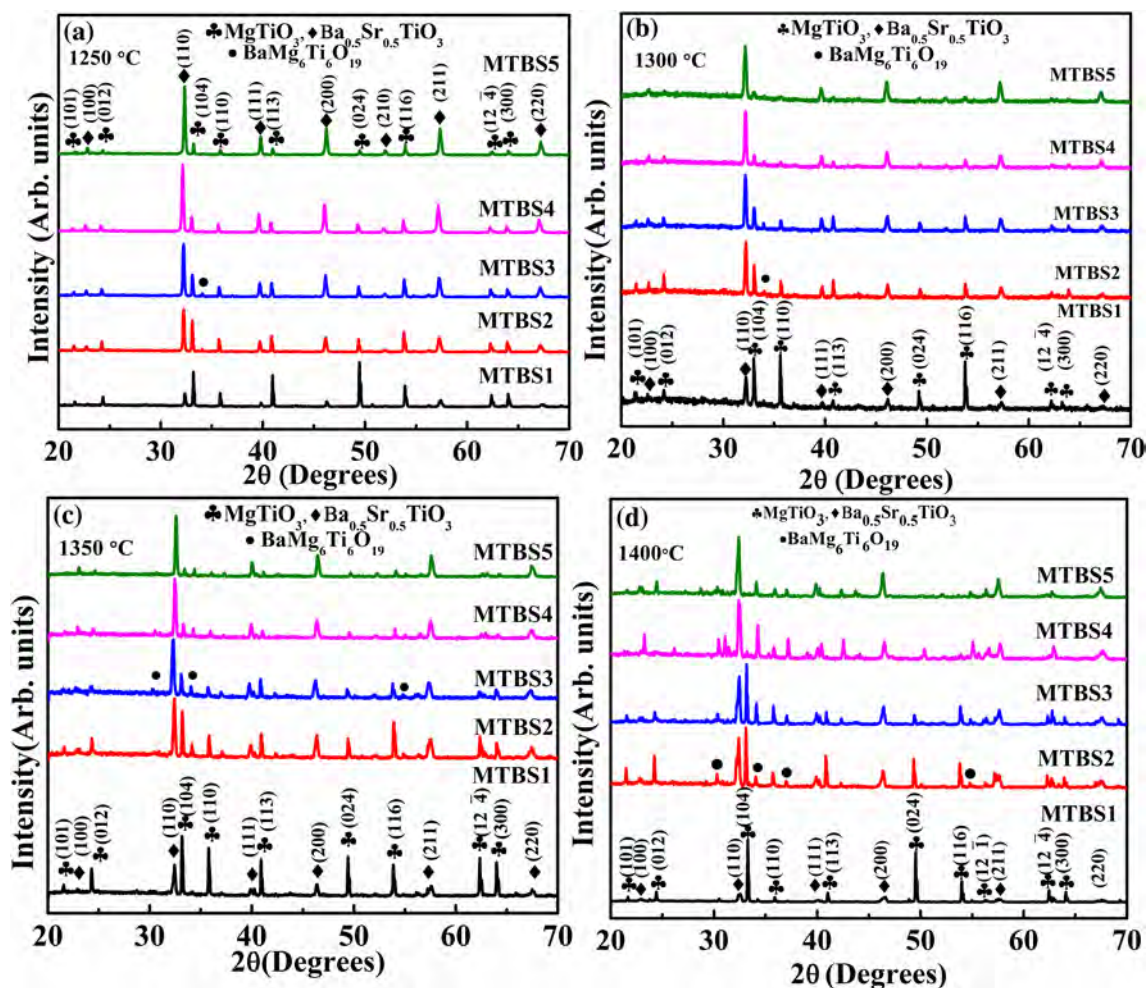


Fig. 1 XRD patterns of MTO-BST composite ceramics sintered at a 1250 °C, b 1300 °C, c 1350 °C and d 1400 °C for 4 h

and MTBS5 had no signature of mixed phases. This clearly indicates that MTO and BST can co-exist independently at those temperatures. On the other hand, MTBS2, MTBS3 and MTBS4 composite ceramics showed a low intensity peak of the mixed phase. The appearance of this phase can be attributed to the similar coordination numbers shared by their cations of these two ceramics. With an increase in sintering temperature from 1250 to 1400 °C leads to a rapid enhancement in the intensities of this mixed phase. This response can be correlate with the induced thermal energy during

sintering that facilitates the growth of mixed phase in these composite ceramics.

In order to understand the effect of sintering temperature on the structural properties of the MTO-BST ceramics, Rietveld refinement had carried out using Fullprof Program by considering the rhombohedral phase of MTO belonging to space group $R\bar{3}$ and cubic phase of BST belonging to $Pm\bar{3}m$ space group. The obtained parameters have listed in Tables 2 and 3 for MTO and BST, respectively. The Rietveld refinement of the XRD patterns for $T_s = 1400$ °C could not

Table 2 Obtained parameter and volume from Rietveld refinement for MTO phase

x	T_s (°C)	a=b (Å)	c (Å)	V (Å ³)	Density(g/cm ³)	χ^2	Relative concentration (%)
0.1	1250	5.0540	13.881	307.067	3.885	5.70	93.1
	1300	5.0542	13.892	307.240	3.890	3.74	91.4
	1350	5.0560	13.905	307.845	3.891	6.50	90.4
0.2	1250	5.0537	13.904	307.489	3.892	4.75	69.6
	1300	5.0537	13.906	307.579	3.894	3.91	63.5
	1350	5.0546	13.905	307.699	3.896	4.85	68.8
0.3	1250	5.0528	13.880	306.891	3.895	4.70	59.0
	1300	5.0531	13.892	307.197	3.902	3.68	63.7
	1350	5.0535	13.900	307.432	3.912	4.70	42.1
0.4	1250	5.0529	13.890	307.266	3.894	3.93	45.8
	1300	5.0528	13.900	307.332	3.896	3.31	37.8
	1350	5.0559	13.904	307.904	3.897	4.18	30.5
0.5	1250	5.0566	13.907	307.948	3.890	3.47	32.0
	1300	5.0551	13.920	308.058	3.897	3.39	33.8
	1350	5.0563	13.920	308.193	3.898	5.35	15.7

Table 3 Obtained parameter and volume from Rietveld refinement for BST phase

x	T_s (°C)	a=b=c (Å)	V (Å ³)	Density (g/cm ³)	χ^2	Relative concentration (%)
0.1	1250	3.9503	61.646	4.943	5.70	6.9
	1300	3.9422	61.262	4.974	3.74	8.6
	1350	3.9419	61.253	4.975	6.50	9.6
0.2	1250	3.9505	61.654	4.942	4.75	30.4
	1300	3.9487	61.569	4.948	3.91	36.5
	1350	3.9431	61.307	4.970	4.85	31.2
0.3	1250	3.9507	61.663	4.941	4.70	41.0
	1300	3.9475	61.513	4.954	3.68	36.3
	1350	3.9444	61.368	4.965	4.70	57.9
0.4	1250	3.9530	61.772	4.933	3.93	54.2
	1300	3.9505	61.654	4.942	3.31	62.2
	1350	3.9497	61.604	4.943	4.18	59.5
0.5	1250	3.9550	61.886	4.923	3.47	68.0
	1300	3.9544	61.836	4.927	3.39	66.2
	1350	3.9524	61.741	4.935	5.35	84.3

be done due to higher concentration and intensity of the mixed phase.

From the Table 2, it is clearly seen that the overall lattice volumes of MTO increases with an increase in sintering temperature from 1250 to 1350 °C. These changes in the lattice volumes might occurred due to the strain exerted by the samples as a result of Ba^{2+} (1.35 Å) substitutions in the MTO lattice. Since, Ba^{2+} (1.35 Å) has larger ionic radii compared to Mg^{2+} (0.720 Å) it is most likely to sit on the interstitial positions of MTO crystal lattice leading to distortion in overall MTO crystal structure. On the other hand, in the case of BST crystals as shown in Table 3, lattice parameters and lattice volumes found to be decreased with an increase in sintering temperature. These results again can be refer to substitution of Mg^{2+} (0.720 Å) in some Ba^{2+} (1.35 Å) and Ti^{4+} (0.605 Å) sites of BST lattice due to similar ionic radii shared by both. Figure 2a–c represents the Rietveld refined plots for $x=0.3$ at different sintering temperatures 1250–1350 °C, respectively and found to be well fitted with the obtained XRD patterns.

As shown in Fig. 2f, the XRD diffraction peaks were shifted towards lower 2θ and get broadened with a rise in sintering temperature from 1250 to 1300 °C for both MTO and BST phase. However, above 1300 °C characteristic peaks of MTO shifted towards lower 2θ without any further peak broadening. Whereas, BST peaks showed only peak broadening. The shifting to lower angle and the broadening of XRD

peaks is attributed to tensile strain and inhomogeneous strain in the ceramics, respectively [15]. To study the lattice strain induced by BST in the MTO-BST composite ceramics, Williamson–Hall (W–H) plots were linearly fitted for MTO and BST phases independently and were presented in Fig. 2d and e, respectively. The average crystallite size and strain for both the phases were calculated from the W–H plots and are listed in Table 4. For both MTO and BST phases, the average crystallite size (L) decreased when the sintering temperature has raised from 1250 to 1300 °C, however, above 1300 °C, crystallite size again enhanced with sintering temperature. The strain (η) in MTO phase was also found to follow the same trend as crystallite size, but in case of BST phase, strain increased with sintering temperature. Both crystallite size and strain, contributes to the broadening of XRD peaks as follows,

$$B_{hkl} = B_{cs} + B_s \quad (6)$$

Table 4 Obtained values of crystallite size (D) and strain (η) for MTO phase from Williamson–Hall plot

T_s (°C)	Crystallite size (Å)		Strain	
	MTO	BST	MTO	BST
1250	950	1969	9.22×10^{-4}	1.89×10^{-3}
1300	655	1201	5.55×10^{-4}	1.91×10^{-3}
1350	2474	1790	1.65×10^{-3}	2.61×10^{-3}

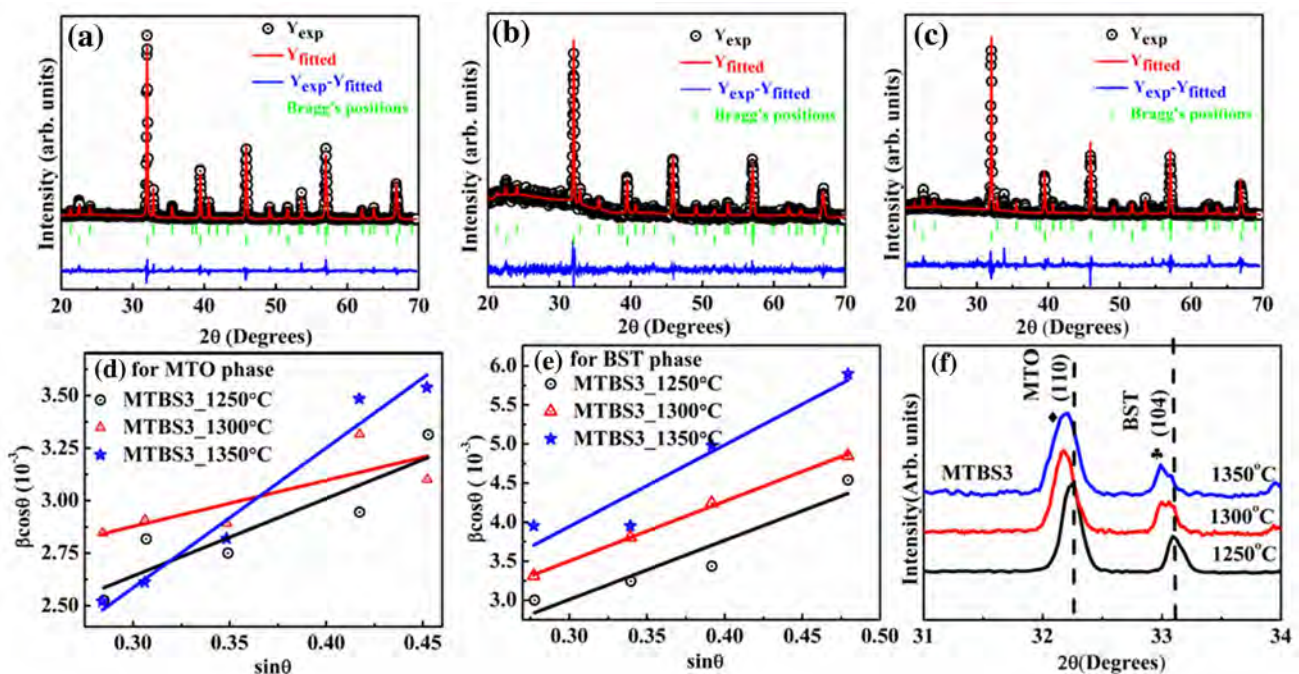


Fig. 2 Rietveld refined XRD patterns of 0.7 MgTiO_3 -0.3 $\text{Ba}_{0.5}\text{Sr}_{0.5}\text{TiO}_3$ (MTBS3) composite ceramics sintered at **a** 1250 °C, **b** 1300 °C and **c** 1350 °C for 4 h and Williamson–Hall plots of **d** MTO

and **e** BST phases at different sintering temperatures for MTBS3 composite ceramics. **f** Magnified XRD spectra for MTBS3 composite ceramics, sintered between 1250 and 1350 °C 4 h

here, $B_{cs} = \frac{k\lambda}{L \cos \theta}$, where, k is a constant (~ 0.94), λ is the wavelength of the X-ray used, θ is the Bragg's angle, L is the crystallite size measured in the perpendicular direction. Similarly, XRD peak broadening from strain (η) in the ceramics, i.e., $B_s = 4\eta \tan \theta$, θ is the Bragg's angle [16]. In the present case, at 1300 °C, thermal energy supplied to disc shaped ceramic composite, induces formation of mixed phase as well as secondary phase, which leads to decrease in both the crystallite size and strain. Further, enhancement in thermal energy leads to abnormal grain growth of all the ceramic phases resulting in enhanced crystallite size and the increased strain can be attributed to presence of multiple phases in the composite ceramics. The XRD analysis of these MTO-BST composites revealed that the sintering temperature had played a significant role in all the variations observed in structural parameters as well as associated strain of the samples. At 1250 °C, densification of samples initiated without formation of mixed phase with minimal strain effect and further rise in sintering temperature induced formation of mixed phase. This might be attributed to thermal energy which is not sufficient for Mg^{2+} and Ba^{2+} to replace Ti^{4+} site in BST lattice and to sit in the interstitial site of MTO lattice, respectively. As, the sintering temperature is raised to 1300 °C, there is sufficient thermal energy to form the mixed phase and this leads to the reduction in the crystallite size due to improvement in strain in the crystals. Further, with increase in the sintering temperature, the intensity of mixed phase as well as crystallite sizes were found to be enhanced.

2.2 Raman spectroscopy

Figure 3a shows Raman spectra of $(1-x)$ MTO- x BST (for, $x=0.1$ to 0.5) composite ceramics, sintered at 1350 °C for 4 h. The effect of composition of composite ceramics on

Raman spectrum is clearly visible from Fig. 3a. For $x \geq 0.3$, ten intense peaks corresponding to the theoretical symmetric (A_g) and antisymmetric (E_g) Raman active modes of MTO are observed along with some minor peaks for BST [17, 18]. In MTO both Mg and Ti are bonded to O by covalent bonds, and it results in high dependency of TiO_6^{4-} and TiO_3^{2-} on Mg . This also signifies the involvement of all atoms in the vibrational modes [19]. In such kind of system, most of the vibrational modes are combinations of symmetry coordinates [20]. However, the MTO modes seemed to be dominating over BST modes for all the compositions and hence to filter out the modes, fitting for Raman spectra were carried out using origin software. The Raman spectra with fitted peaks is shown in Fig. 3b and details of the peaks position and peak properties are presented in Table 5. To study the effect of sintering temperature, Raman spectra for

Table 5 Obtained Raman shift peak and corresponding FWHM for MTBS3 composite ceramics sintered at 1350 °C

Serial no	Peak position (cm^{-1})	FWHM (cm^{-1})
1	179.06 ± 1.02	18.16 ± 2.03
2	229.63 ± 0.05	4.51 ± 0.03
3	233.71 ± 1.13	23.51 ± 2.23
4	286.22 ± 0.02	3.72 ± 0.04
5	310.99 ± 0.15	5.88 ± 0.04
6	332.74 ± 0.03	4.13 ± 0.07
7	357.87 ± 0.03	6.87 ± 0.08
8	402.21 ± 0.06	4.33 ± 0.15
9	490.48 ± 0.10	7.61 ± 0.34
10	505.13 ± 0.71	12.45 ± 2.50
11	576.16 ± 1.81	26.71 ± 3.25
12	644.46 ± 0.39	10.39 ± 1.02
13	719.17 ± 0.01	21.39 ± 0.40
14	754.92 ± 1.25	54.34 ± 0.20

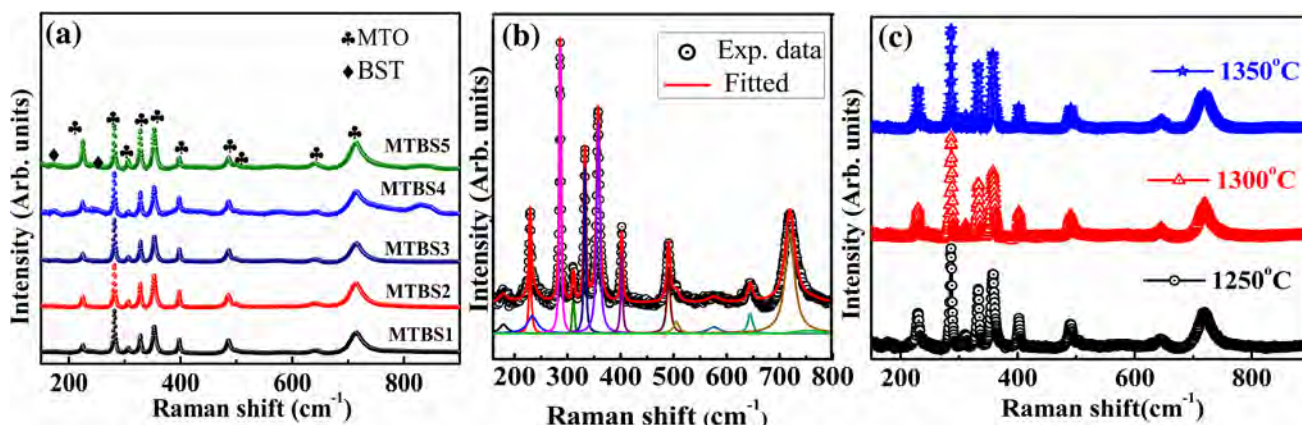


Fig. 3 Raman spectra of **a** MTO–BST composite ceramics sintered at 1350 °C and **b** Fitted Raman spectra for MTBS3 sample sintered at 1350 °C for 4 h. And **c** MTBS3 sintered at different sintering temperatures

MTBS3 composite ceramics, sintered at three different temperatures are plotted and are shown in Fig. 3c. However, no significant changes observed in Raman spectra with sintering temperature.

The mode at A_g (229 cm^{-1}) and A_g (311 cm^{-1}) corresponds to vibration of Mg^{2+} and Ti^{4+} ions along z axis, whereas, A_g (402 cm^{-1}), A_g (505 cm^{-1}) and A_g (719 cm^{-1}) are due to independent vibration of O^{2-} ions. The A_g (505 cm^{-1}) and A_g (719 cm^{-1}) modes exhibited the symmetric breathing like vibrations of six O^{2-} ions corresponding to different degrees of freedom of oxygen octahedron. In the case of E_g modes, the E_g (286 cm^{-1}) originated from anti-symmetric breathing vibrations of oxygen octahedron. The E_g (332 cm^{-1}) and E_g (357 cm^{-1}) modes represented twisting of oxygen octahedron with the vibrations of the Mg^{2+} and Ti^{4+} ions parallel to X – Y plane. The E_g (490 cm^{-1}) and E_g (644 cm^{-1}) modes belong to combination of antisymmetric breathing and twisting vibrations of oxygen octahedral with the cationic vibrations parallel to the X – Y plane. For E_g (490 cm^{-1}) mode both Mg^{2+} and Ti^{4+} ions are involved in the vibrations, while the E_g (644 cm^{-1}) mode primarily involves Mg^{2+} . Raman modes for BST observed at 179 cm^{-1} may originated from A site ions oscillation due to Mg^{2+} ion substitution [21]. Raman peak at 233 cm^{-1} is attributed to the rotations of the oxygen cage and ordering of B site ions [22], while the broad peak at 576 cm^{-1} originates from TiO_6 octahedron stretching.

2.3 Microstructural properties

The surface micrographs of $(1-x)\text{MTO}-x\text{BST}$ (for, $x=0.1$ to 0.5) sintered composite ceramics at $1300\text{ }^\circ\text{C}$ for 4 h, were obtained by FESEM and are presented in Fig. 4a–e. Grains of two distinct sizes were observed from the FESEM micrographs. One type of grains are comparatively larger in size $\sim 2\text{--}3\text{ }\mu\text{m}$, whereas the another type grains are less than $1\text{ }\mu\text{m}$ in size. All the samples have shown well packed microstructures. The number of smaller grain also increases as the BST concentration increases in the samples. At the same time the grain with larger sizes also become smaller with an increase in BST concentration, which might be attributed to uniform mixing of BST-MTO ceramics and BST grains would act as a barrier between MTO grains for further growth [23]. From the above observations it can be concluded that larger grains are composed of MTO and smaller grains are composed of BST ceramic phases. As shown in the Fig. 4f, elemental distribution on a large area of the ceramics is found to be nearly equal to the calculated value. With addition to it the EDS analysis also confirmed that grain A and B belongs to MTO and BST ceramics, respectively. Further, to study the effect of sintering temperature on the microstructural properties of MTO-BST ceramics the FESEM images of MTBS3 samples, sintered at 1250 to $1350\text{ }^\circ\text{C}$ are

obtained and are shown in Fig. 5a–c. An enhancement in the grain size as well as packing of grains have observed with an rise in sintering temperature. At $1350\text{ }^\circ\text{C}$, MTBS3 exhibited highly compact and uniform microstructure.

The density plays a significant role in dielectric properties of a ceramic composite. The relative density of the ceramics was estimated by Archimedes method and the relative densities are found to be $\sim 95\%$, $\sim 95.8\%$ and $\sim 97\%$ for the composites sintered at 1250, 1300 and $1350\text{ }^\circ\text{C}$, respectively. The relative densities of all the composite ceramics sintered at $1350\text{ }^\circ\text{C}$ are given in Table 6.

2.4 Microwave dielectric properties

To study the effect of BST on MTO, the microwave dielectric parameters of the composite ceramics were extracted at a spot frequency by using Hakki–Coleman method considering TE_{011} mode. Hakki–Coleman configuration, consists of a cylindrical dielectric post sandwiched between two infinite conducting plates. In which $TE_{01\delta}$ modes, the fields outside the resonator decays very rapidly and hence, the effect of air gap between dielectric resonator and conducting plates becomes negligible. The BST ceramic was found to have significant effect on the microwave dielectric properties of the MTO-BST composites. The obtained microwave parameters are summarized and plotted in Table 6 and Fig. 6, respectively. The Q value and the resonant frequency for the composites were found to be decreased with an increase in BST concentration. Whereas, dielectric permittivity value has shown a significant enhancement with BST concentration. The $Q \times f_0$ value of the composite ceramics exhibited drastic change from $\sim 17,806$ to 988 GHz for $x=0.1$ to 0.5, respectively. The observed degradation in Q value may be attributed to relaxation polarization present in BST at higher frequencies [23]. The resonant frequency (f_0) has also showed dependency on BST concentration and varied from 7.262 to 2.54 GHz for, $x=0.1$ to 0.5. At, microwave frequency range the MTBS composites exhibited much higher dielectric permittivity as compared to pure MgTiO_3 and recorded maximum of ~ 200 for MTBS5. At, the same time, enhancement in dielectric loss ($\tan\delta$) also noticeable with increase in BST concentration, which is also an important parameter for application point of view. An optimization of all dielectric parameter is required in this composite ceramics study. Hence, MTBS1 with $x=0.1$, composite ceramics exhibited the best microwave dielectric properties with dielectric permittivity of $\epsilon_r \approx 20$, dielectric loss of $\sim 10^{-4}$ and $Q \times f_0 \sim 17,806$ at 7.262 GHz. Further, the quality factor ($Q \times f_0$) of the MTBS composite ceramics also found to be enhanced from 7800 to 17,806 GHz with sintering temperature from 1250 to $1350\text{ }^\circ\text{C}$. This improvement in quality factor ($Q \times f_0$) value with sintering temperature can be attributed to increased relative density with sintering temperature,

Fig. 4 FESEM micrographs of MTO-BST composite ceramics are shown from (a) to (e) for MTBS1–MTBS5, respectively, sintered at 1300 °C for 4 h. **f** EDS elemental distribution spectra of the MTBS3 composite at selected area

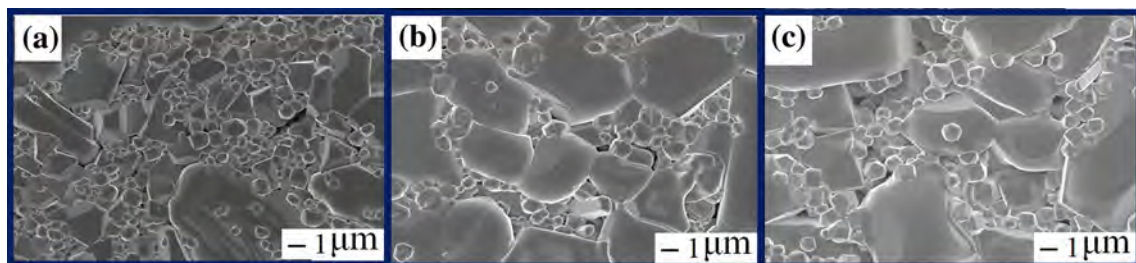
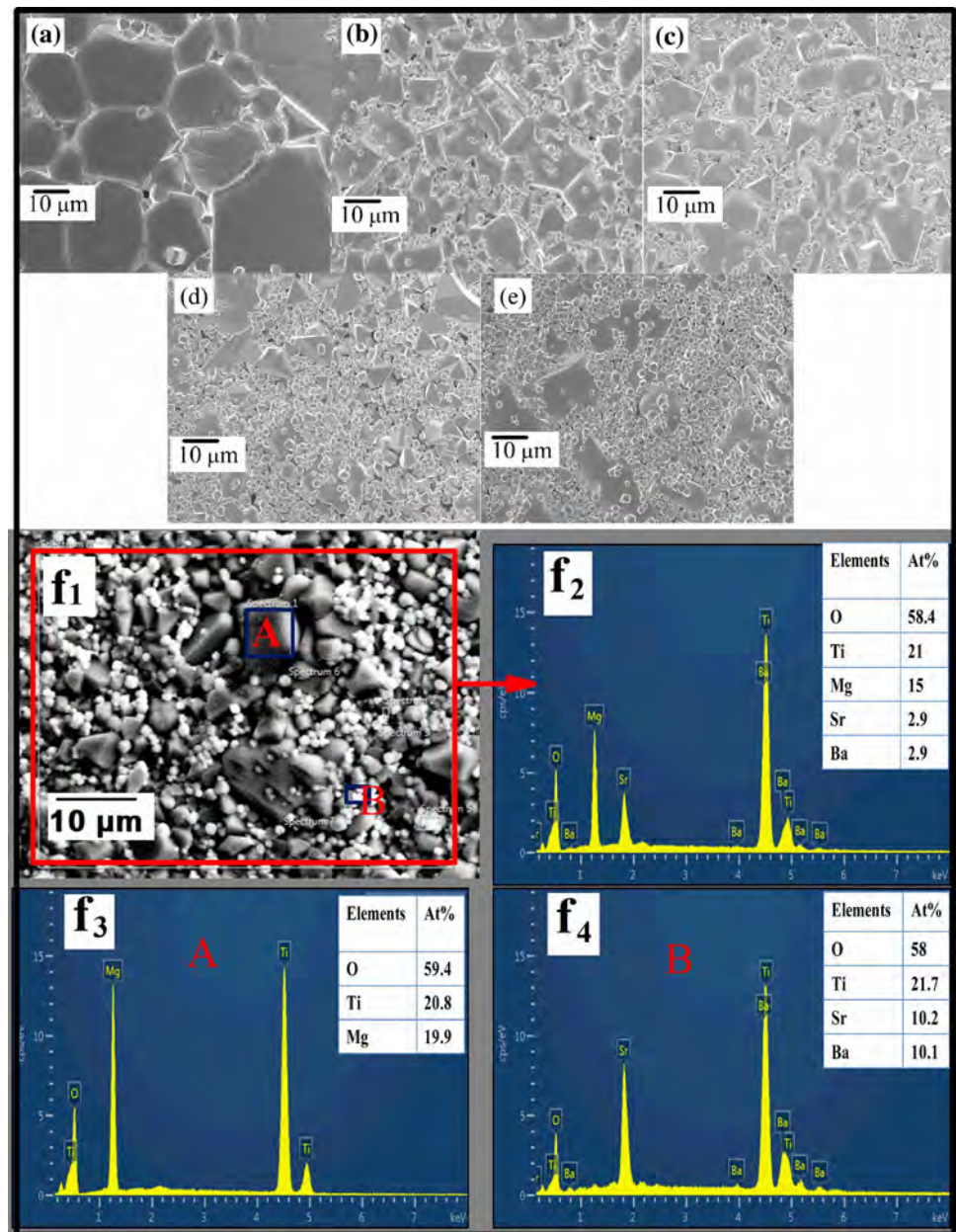
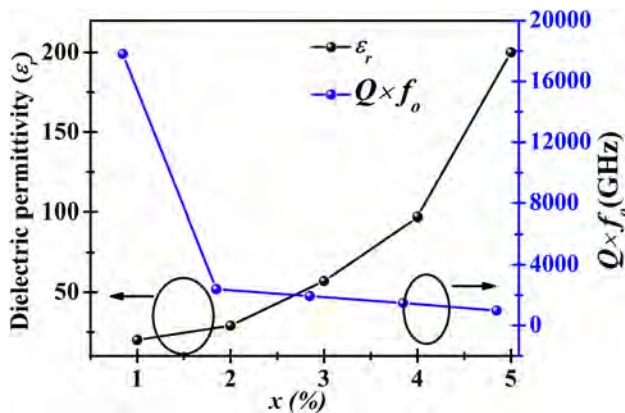


Fig. 5 a–c FESEM images of MTBS3 composite ceramics sintered at 1250 °C, 1300 °C and 1350 °C for 4 h, respectively

Table 6 Obtained Microwave and dielectric parameters of MTO-BST composite ceramics sintered at 1350

Sample name	Resonant frequency (GHz)	Dielectric permittivity (ϵ_r)	Quality factor (Q)	$Q \times f_o$ (GHz)	Relative density (%)	T_C (°C)	Maximum relative dielectric permittivity (ϵ_m)	Diffuseness co-efficient (γ)
MTBS1	7.262	20 ± 0.2	2452	17,806	97.90	−81	22	1.002
MTBS2	4.928	29 ± 0.3	486	2395	97.84	107	50	1.574
MTBS3	4.160	57 ± 0.57	464	1930	97.69	−62	153	1.822
MTBS4	3.686	97 ± 0.97	400	1474	97.30	−51	605	1.821
MTBS5	2.548	200 ± 4	388	988	97.06	−50	676	1.834

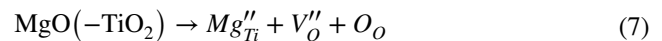
**Fig. 6** Variation of dielectric permittivity and $Q \times f_o$ value with BST concentration

which will result in less conduction loss through the defect states originated from porous microstructure of the ceramics [6]. It is interesting to note that the addition of BST has significantly influenced the microwave dielectric properties. There is a drastic improvement in the dielectric constant at the same time the quality factor degraded as compared to pure MTO [24].

2.5 Broadband dielectric properties

In Fig. 7, dielectric responses of MTBS composite ceramics as a function of temperature measured at different frequencies are demonstrated. Unlike pure MTO and BST ceramics, MTBS and pure BST ceramics has exhibited diffused transition. Due to the addition of BST ceramics in MTO ceramics, the dielectric constant showed an overall enhancement as well as a transition with temperature. The dielectric constant value has found to be increased abruptly from $x=0.3$ to 0.4 as compared to $x=0.1$ to 0.3 and this can be attributed to actual individual phase concentrations in the composite ceramics as estimated from Rietveld refinement. As the BST concentration increases the transition peak become more prominent and the transition temperature (T_C) value shifted towards BST's T_C . These responses indicated

a mixed dielectric contribution from both the phases in the MTO-BST composite ceramics. From the earlier studies it is evident that due to replacement of Mg^{2+} in the acceptor site of ABO_3 , transition temperature of BST shifts towards lower temperature. When Mg replaces Ti on the B site of perovskite ABO_3 structure and a double ionized oxygen vacancy is formed simultaneously, i.e.,



Mg ions along with charged oxygen vacancies induces the local deformation in the perovskite unit cells leading to the reduction of the tetragonal c/a ratio and hence, the Curie temperature T_C shifts towards lower temperature [10]. For 10 mol% BST composite, the dielectric transition is highly diffused in nature, which has exhibited a broad peak T_C . In the present study, the dielectric constant has exhibited diffused kind of transitions with measurement temperature for all the MTBS composite ceramics and such kind of transition is a signature of relaxor ferroelectrics [25–27]. Further, for the first time two scientists Uchino and Nomura proposed a modified Curie–Weiss law, to probe the nature of this relaxor behaviour of ferroelectrics [28]. The modified Curie Weiss law can be express

$$(1/\epsilon_r - 1/\epsilon_m) = \frac{(T - T_C)^\gamma}{C} \quad (8)$$

where C is the Curie constant, γ is diffuseness constant and ϵ_m is the maximum dielectric constant at T_C . Again, the numerical value of diffuseness constant γ lies between 0 and 1 and 1 to 2 for perfect ferroelectric and relaxor ferroelectric materials, respectively. In Fig. 8, the plots for, $\log(1/\epsilon_r - 1/\epsilon_m)$ versus $\log(T - T_C)$ are shown and the value of γ has been extracted from slope of the linearly fitted lines for all the MTBS composite ceramics at 1 MHz. The obtained γ values varied from 1.01 for $x=0.1$ to 1.83 for $x=0.5$, as a indication of relaxor nature of the ceramics as given in the Table 6. The diffuseness constant γ has found to be enhanced with an increase in x , which can be attributed to larger amount of distortion in the sample.

Figure 9, corresponds to dielectric loss ($\tan\delta$) as a function of measuring temperature at various frequency of the

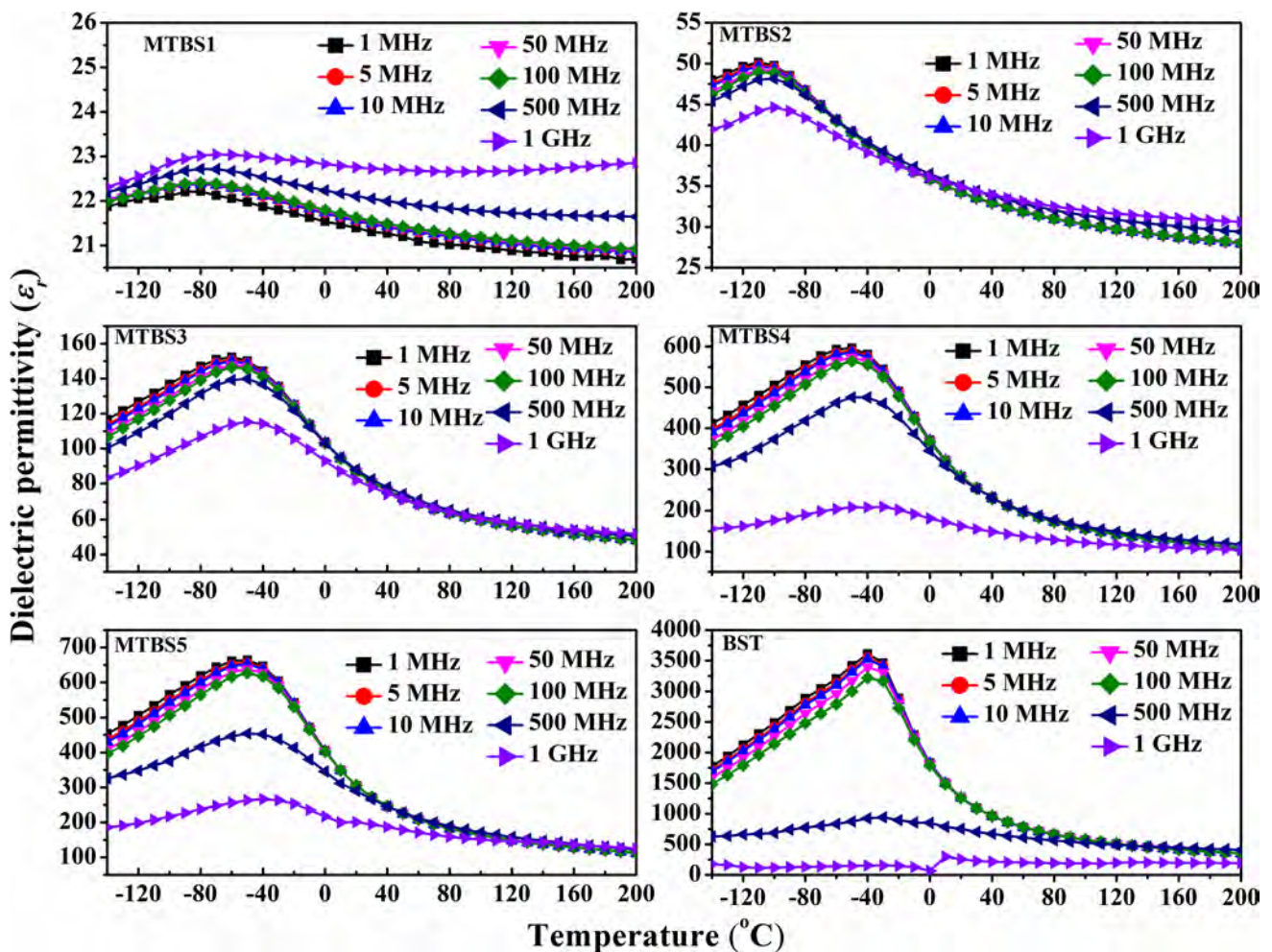


Fig. 7 Broadband (1 MHz– GHz) dielectric response of MBST ceramics as a function of temperature for MTO–BST composite and pure BST ceramics, respectively

MTBS composite ceramics. The dielectric loss ($\tan\delta$) also enhanced due to addition of BST ceramics in the MTO matrix. The dielectric loss ($\tan\delta$) has showed distinct anomaly near the T_C for all the composite ceramics. For all the composite ceramics, it has observed that the peak of dielectric loss shifts towards higher temperature and overall value also increased with a rise in the measurement frequency. As per earlier studies, these behavior of dielectric loss is related to dielectric relaxation process and the value of dielectric loss implies the concentration of dielectric relaxation units [29].

The MTBS3 sample with $x=0.3$, was optimized for further study due to its better structural and microstructural properties. Figure 10a shows the variation of dielectric permittivity as a function of temperature measured at different frequencies (1 kHz to 100 kHz) for MTBS3 composite ceramic. The MTO–BST composite ceramics have shown significant dependency on temperature, which can be attributed to temperature dependent dielectric

permittivity of BST ceramics. It is observed that there are two regions for temperature dependent dielectric permittivity for all the frequency range. From room temperature to 200 °C, dielectric permittivity decreases with measurement temperature but with further rise in temperature there is an improvement in the permittivity, which can be attributed to the phase transition associated to BST phase near room temperature as shown in the previous analysis and thermally activated polarization in the high temperature region ($T > 200$ °C). Figure 10b and c displayed the dielectric permittivity with frequency in two different temperature ranges (RT to 250 °C and > 250 °C). In the lower temperature region (RT to 250 °C), dielectric permittivity has shown minimal variation with frequency, whereas, in the higher temperatures and at lower frequencies the permittivity exhibited higher values, due to the contribution of space charge polarization and gradually decrease with frequency and become almost constant as a function of frequency.

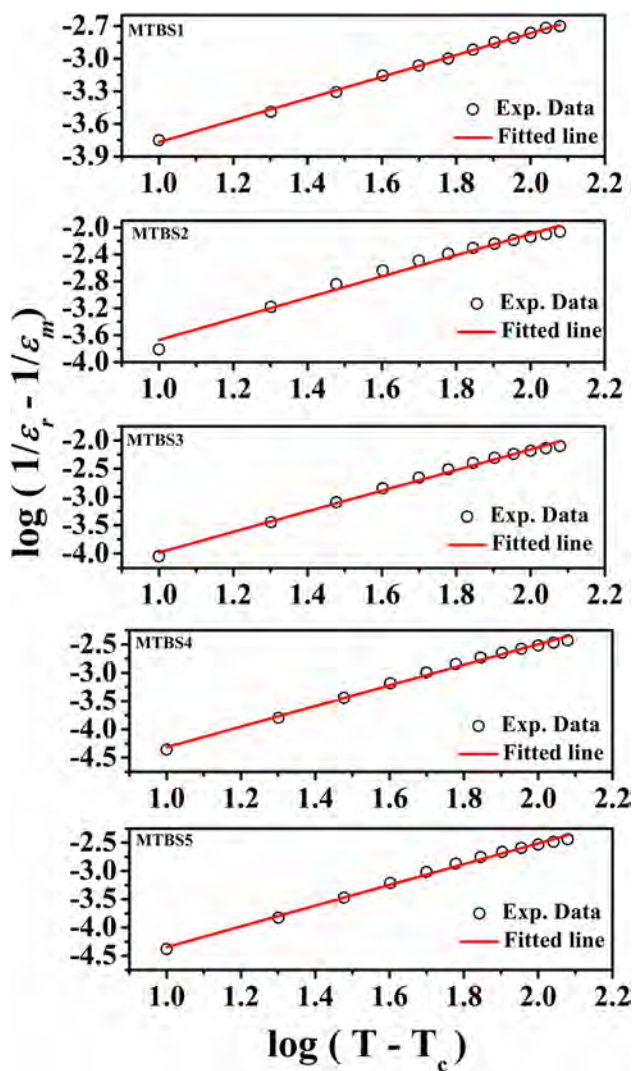


Fig. 8 The plots of $\log(1/\epsilon_r - 1/\epsilon_m)$ versus $\log(T - T_c)$ for MTO-BST composite ceramics

The variation in dissipation factor as a function of frequency (1 kHz to 100 kHz), measured at different temperatures is shown in Fig. 11a. The dissipation factor of the sample exhibited relaxation type of behavior with a broad peak and the shift of the peak value towards higher frequency with an increase in temperature indicates the strong dispersion in dissipation factor of the sample due to dipole relaxation. And the relaxation time can be described by Arrhenius law, i.e.,

$$\omega_n = \omega_0 \exp \left[\frac{-E_a}{k_B T} \right] \quad (9)$$

where ω_m , ω_0 and E_a denotes the angular frequency for maximum value of dissipation factor, pre-exponential factor and activation energy of the sample, respectively.

Further, Fig. 11b, shows the variation of $\log \omega$ with $1000/T$, where solid line is the linearly fitted. The activation energy is calculated from the slope of the fitted line and is found to be 1.12 eV. The obtained activation energy is associated with thermally activated conduction of charge carriers across the grains and grain boundaries. The activation energy (E_a) for conduction around 1 eV corresponds to the migration of oxygen vacancies in perovskites [30, 31]. The dielectric relaxation behavior at higher temperature corresponds to short range hopping of oxygen vacancies. In the current study the activation energy value signifies presence of conduction by doubly ionized oxygen vacancies in the samples [32, 33].

Figure 12a shows the spectra of the imaginary part of impedance vs frequency at different measurement temperatures (30 to 400 °C). The imaginary part of impedance is very high in lower frequency region and decreases with an increase in frequency. But towards higher frequency region, the spectra merged together for all the measured temperatures. At higher frequencies, the drop in imaginary part of impedance is due to release of space charge carriers [34]. This independency of impedance with frequency in the high frequency region also implies an enhancement in ac conductivity with temperature [35].

Electrical properties exhibited by the ceramics are a compound effect of conduction at various electrically active regions like grains and grain boundaries [36]. This mechanism in ceramics can be understood by Brick-layer model [37]. In impedance spectroscopy, Brick-layer model is used to understand conduction in grains and across the grain boundaries. In polycrystalline, multigrain system the resistivity of grain boundaries can be considered larger than the resistivity of core grains and can be expressed as an two components equivalent electrical circuit consisting of a parallel capacitor (C) and resistor (R) connected in series.

The complex impedance spectrum is a representation of various relaxation phenomenon associated with the sample. On the basis of such responses, a number of phenomenon were introduced by Debye, Cole–Cole, Cole–Davidson, Havriliak–Negami etc. All these models can be categorized broadly into Debye and non-Debye type of relaxation representing non-interacting (one body) and interacting (many body) system. In Debye type, dipoles will not have any interaction with each other as they are separated by a viscous medium. On an application of electric fields, these dipoles will align along the field direction and on removal of the field, the dipoles will reorient back to their initial position. In such cases, impedance spectra will be a perfect semicircle, originating from real axis. But, usually all practical systems are non-Debye type, where there will be interactions among the dipoles present in the system and hence the impedance spectra will be a distorted semicircle originating below the real axis. The impedance spectra in the present case showed Cole–Cole type relaxation

Fig. 9 a–e Dielectric loss ($\tan\delta$) as a function of measuring temperature at various frequency of the MTBS composite and BST ceramics

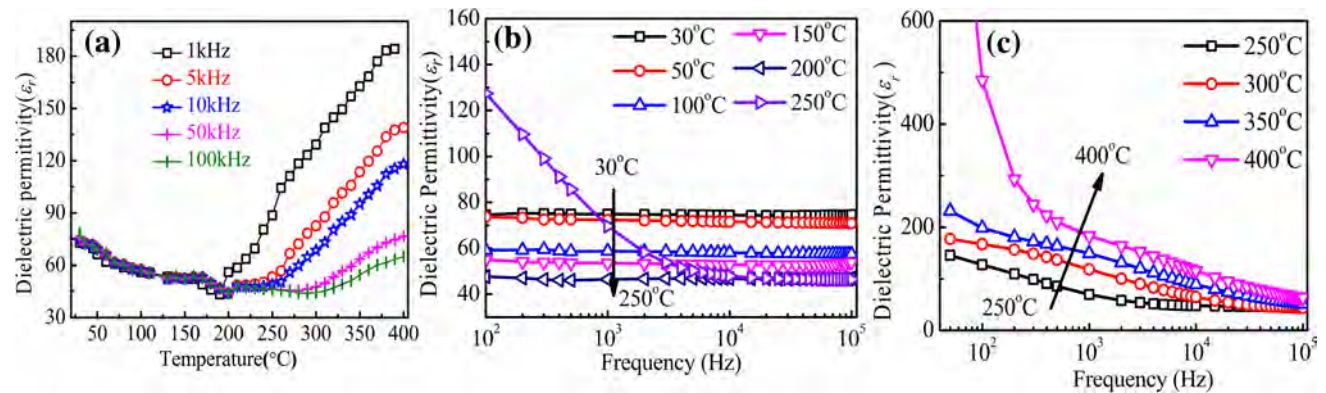
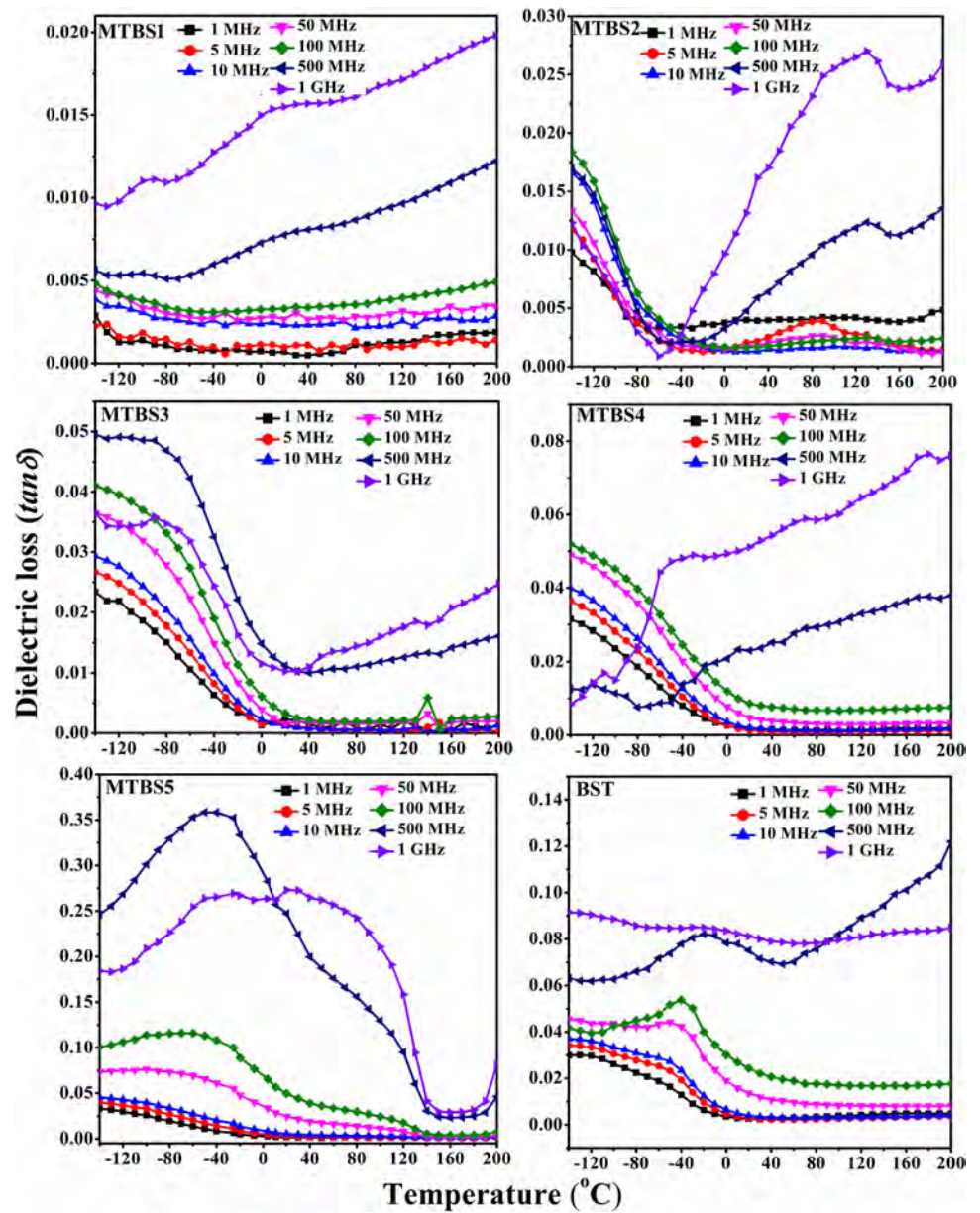


Fig. 10 a Dielectric permittivity variation as a function of temperature measured at different frequencies and dielectric permittivity spectra as a function of frequency measured at different temperatures b RT to 250 °C and c T > 250 °C, respectively

behavior. The mathematical equation for Cole–Cole type for dielectric constant $\epsilon(\omega)$ at angular frequency ω is can be express as,

$$\epsilon(\omega) - \epsilon(\infty) \propto \frac{1}{(1 + i\omega\tau)^{1-\alpha}} \quad (10)$$

where $\epsilon(\infty)$ and α represent permittivity at high frequency and angle of deviation below real axis, respectively. In present case, relaxation phenomenon is analyzed in the impedance plane using the following equations relating permittivity and impedance,

$$\epsilon'' = \frac{Z'}{\omega C_0 (Z'^2 + Z''^2)} \quad (11)$$

$$\epsilon' = \frac{-Z''}{\omega C_0 (Z'^2 + Z''^2)} \quad (12)$$

Fig. 11 **a** Variation of dissipation factor (D) with frequency measured at different temperature and **b** $\ln\omega_{\max}$ versus $1000/T$ plot from dissipation spectra

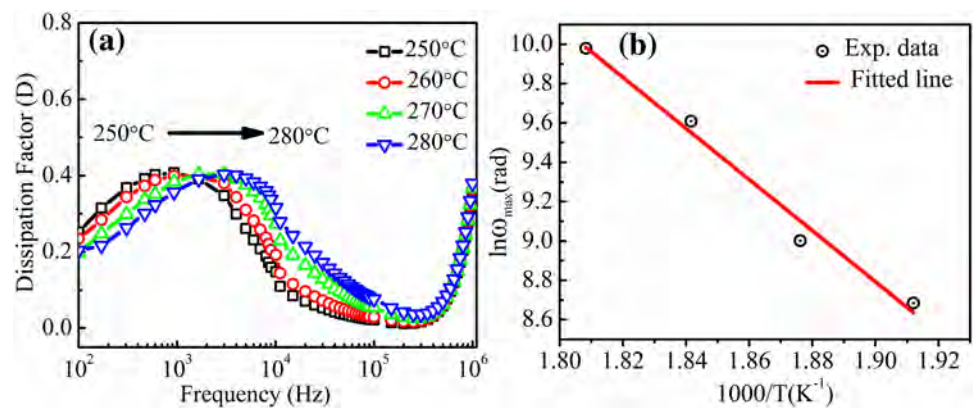


Fig. 12 **a** Spectra of imaginary part of impedance as a function of frequency at different measurement temperature and **b** Fitted complex impedance spectra and corresponding equivalent electrical circuit given in the inset

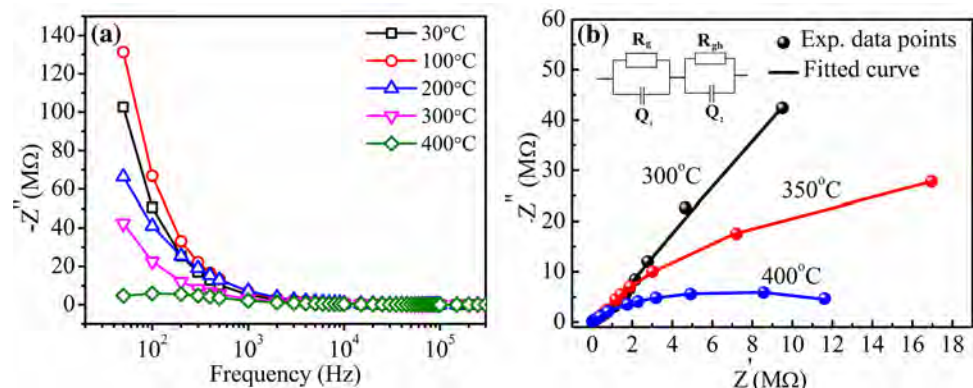


Table 7 The numerical values of resistance and capacitance for MTBS3 extracted from Cole–Cole-plot

Temperature (°C)	R_g (M Ω)	Q_1		Q_2		R_{gb} (M Ω)
		$A_1 (\times 10^{-10})$	n_1	$A_2 (\times 10^{-10})$	n_2	
300	3910	1.557	0.873	9.175	0.964	0.377
350	83.26	9.157	0.769	10.880	0.908	0.317
400	14.14	11.63	0.767	2.462	0.898	0.133

where C_0 is the vacuum capacitance. The complex impedance spectra at three different temperatures are fitted using Cole–Cole model circuit. The equivalent circuit for the sample obtained using this model is shown in the inset of the Fig. 12b. The numerical values of circuit elements are tabulated in Table 7, where Q represents the constant phase element that can behave either as a capacitor or a resistor, depending on n is 0 or 1. The obtained bulk resistance for the circuit is found to be decreased with an increase in temperature, which is a signify negative co-efficient of resistivity. The drop in resistance towards higher temperature occurs due to the release of charges accumulated at the grain boundaries and electrode interfaces contributing to conductivity in the sample [36].

In dielectric ceramics, the loss (dissipation) occurs as a result of conduction in the sample. Thus, the real part of

conductivity (σ) can be express in terms of dielectric loss (ϵ'') as,

$$\sigma = \omega \epsilon_0 \epsilon'' \quad (13)$$

where ω and ϵ_0 are angular frequency and dielectric permittivity in free space, respectively [38]. Ideally, in ceramic systems conductivity diminishes with decrease in frequency and shows a constant value after a certain frequency. The region where conductivity becomes independent of frequency is referred as DC conductivity (σ_{dc}). In general, the AC conductivity shows a direct proportionality with frequency and the real part of such conductivity obeys a Power law, known as Almond-West relation, i.e.,

$$\sigma = \sigma_{dc} \left[1 + \left(\frac{\omega}{\omega_H} \right)^n \right] \quad (14)$$

where ω_H denote hopping frequency of charge carriers and n is the Joncher's constant [36]. In AC conductivity if $n \leq 1$, the conduction process follows an ideal ionic process of Debye dielectric dipolar type [38]. For such processes, charge carrier conduction occurs via hopping motion. For the other case, when $n > 1$, localized long range back and forth hopping of charge carriers is present [39, 40]. The frequency dependent conductivity spectra of MTBS3 at different measurement temperature is showed in Fig. 13a and which can be divided into two regions, frequency independent plateau (Region I) and dispersion region (Region II). The frequency independent plateau region corresponds to dc conductivity σ_{dc} and its numerical value can be obtained by extrapolating the curve towards lower frequency. The frequency dependence of conductivity in dispersive region can be express by using Joncher's universal power law [41] i.e.,

$$\sigma_{tot} = \sigma_{dc} + \sigma_{ac} \quad (15)$$

$$\sigma_{ac} = A\omega^s \quad (16)$$

where A is pre-exponential factor and $\omega = 2\pi f$ is angular frequency and ' s ' is power law exponent (ideally, $0 < s < 1$). The dispersive regions were fitted into two different frequency

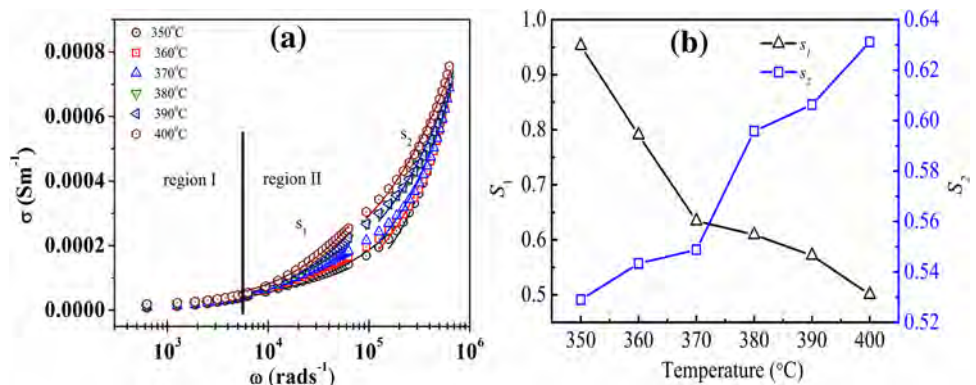
regions and the obtained variation of s values with measurement temperature showed in Fig. 13b. The dependency of ' s ' value with temperature is also can be relate to the different conduction mechanisms associated with the sample. Temperature independent ' s ' implies quantum mechanical tunneling (QMT) of charge carriers, ' s ' will be enhanced with increasing T in case of small polaron conduction mechanism and for correlated barrier hopping (CBH) model ' s ' would improve with reduction in T and tends to unity at 0 K [42]. The obtained values of s_1 ($1 \text{ kHz} < \omega < 100 \text{ kHz}$) and s_2 ($100 \text{ kHz} < \omega < 1 \text{ MHz}$) are in the range of 0 to 1. Whereas, the values of s_1 decreases with rise in temperature and s_2 enhanced with an increase in temperature. The obtained values imply the ac-conductivity of the test sample comprises of both small polaron and correlated barrier hopping mechanisms. In the low frequency region ' s_1 ' signifies translational hopping and in the higher frequency region s_2 characterizes the presence of localized relaxation [43].

The change in capacitance over a measurement temperature is an important parameter for a dielectric capacitors. The change in capacitance evaluated from capacitance versus temperature (-30 to $+125$ °C) curve shown in Fig. 14 and found to be $\sim 54\%$ over the temperature range of (RT) -30 to $+85$ °C. This obtained value of change in capacitance fulfills the criteria for type-II capacitor [4].

3 Conclusions

$(1-x)\text{MgTiO}_3-x\text{Ba}_{0.5}\text{Sr}_{0.5}\text{TiO}_3$ (for $x=0.1$ to 0.5) composite ceramics were successfully prepared by solid state reaction method. The XRD results also revealed presence of mixed phase # $\text{BaMg}_6\text{Ti}_6\text{O}_{19}$ apart from independent phases of MTO and BST. The intensities of mixed phase were found to be enhanced with an increase in BST concentration as well as sintering temperatures. The Raman spectra also complements with the XRD results. The microstructures of the composites were also showed dependency on BST concentration as well as sintering temperature. The sintering temperature of the MTO-BST composite ceramics is optimized as 1350 °C, and the dielectric permittivity is found to be

Fig. 13 Frequency dependent conductivity with frequency at different measurement temperature



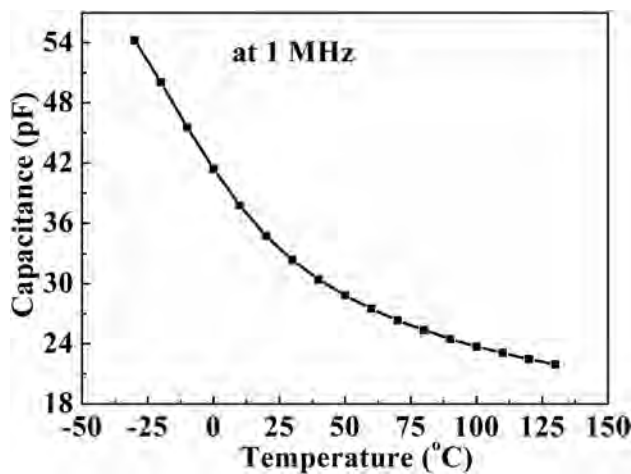


Fig. 14 Capacitance vs temperature curve for MTBS3 composite ceramics at 1 MHz

in the range of $\epsilon_r \approx 20$ –200, dielectric loss $\sim 10^{-4}$ – 10^{-3} and $Q \times f_0 \sim 17,806$ GHz at 7.262 GHz to 988 GHz at 2.548 GHz. The temperature dependent dielectric constant for the composite ceramics have exhibited diffused transition as a typical signature of relaxor ferroelectrics due to compound response of ferroelectric BST and linear dielectric MTO. The diffuseness constants extracted by modified Curie–Weiss law are found to be 1.002 for $x=0.1$ and 1.834 for $x=0.5$, respectively. All the characterizations and analysis MTBS3 sintered at 1350 °C is optimized exhibited the best behavior with enhanced dielectric permittivity $\epsilon_r \approx 57$, loss of $\sim 10^{-3}$ and $Q \times f_0 \sim 1,930$ at 4.16 GHz. The obtained value of dielectric permittivity is much higher than MTO ceramics and lower than pure BST ceramics, which may be attributed to compound response of dielectric polarization from both MTO and BST grains as well as grains of mixed phase $\text{BaMg}_6\text{Ti}_6\text{O}_{19}$ ceramics. The Impedance analysis revealed the presence of non-Debye type conductivity relaxation in the sample. The thermal stability of capacitance have been estimated over the temperature range of (RT) – 30 to +85 °C and found to be $\sim -54\%$. The optimized MTBS3 composite has exhibited high dielectric permittivity with low loss tangent value and temperature stable capacitance favorable for type-II capacitor in IC applications.

Acknowledgements The authors acknowledge the financial support and facilities provided by DAE BRNS [37 (1)/14/33/2015/BRNS]. The authors acknowledge Central Instruments facility, IIT Guwahati, for providing Raman Spectroscopy, FESEM and RF Impedance analyzer system. The authors also acknowledge, Centre for Nanotechnology, IIT Guwahati, for FESEM images. SR would like to acknowledge Gohonzon and family for constant support throughout the work.

References

1. A.K. Tagantsev, et al., *J. Electroceram.* **1**, 5 (2003)
2. L.C. Sengupta, S. Sengupta, *IEEE Trans. Ultrason. Ferroelectr. Freq. Control* **44**, 792 (1997)
3. V.O. Sherman, *J. Appl. Phys.* **99**, 074104 (2006)
4. http://www.calramic.com/Design/Assets/PDF_files/AN110-Voltage-Temperature-Coefficient.pdf
5. http://www.electronics-notes.com/articles/electronic_components/capacitors/ceramic.php
6. T. Santhosh Kumar, et. al., *Mater. Sci. Eng. B* **194**, 86–93 (2015)
7. S.S. Gevorgian, E.L. Kollgerg, *IEEE Trans. Microwave Theory Tech.* **49**, 2117 (2001)
8. L.C. Sengupta, S. Sengupta, *Mater. Res. Innov.* **2**, 2278 (1999)
9. B. Su, T.W. Button, *J. Appl. Phys.* **95**, 1382 (2004)
10. S. Ke, H. Fan, et al., *Compos. Part A* **39**, 597 (2008)
11. A.R. West, et al., *J. Electroceram.* **1**, 65 (1997)
12. B.W. Hakki, P.D. Coleman, *IEEE Trans. Microwave Theory Technol.* **8**, 402 (1960)
13. W.E. Courtney, *IEEE Trans. Microwave Theory Technol.* **18**, 476 (1970)
14. M.T. Sebastian, *Dielectric Materials for Wireless Communications* (Elsevier Science Ltd, Netherlands, 2008)
15. Birkbeck College, University of London. <http://pd.chem.ucl.ac.uk/pdnn/peaks/size.htm>
16. V.D. Mote, *Journal of Theoretical and Applied Physics* **6**[1], 6 (2012)
17. W. Chun-Hai, et al., *J. Appl. Phys.* **104**, 034112 (2008)
18. J. Zhang, et al., *J. Appl. Phys.* **104**, 084102 (2008)
19. B. Reynard, F. Guyot, *Phys. J. Chem. Miner.* **21**, 441 (1994)
20. D.C. Harris, M.D. Bertolucci, *Symmetry and Spectroscopy: An Introduction to vibrational and Electronic Spectroscopy* (Oxford University Press, New York, 1978), pp. 170–173
21. M. Osada, et al., *J. Appl. Phys. Lett.* **75**, 3393 (1999)
22. H. Zheng et al., *J. Eur. Ceram. Soc.* **23**, 2653 (2003)
23. Z. Cheng, et al., *Phys. Rev. B* **77**, 092101 (2003)
24. J. Sun, X. Chou, et al., *Ferroelectrics* **356**, 128 (2009)
25. L. Eric Cross, *Ferroelectrics* **151**, 305 (1994)
26. L. Eric Cross, *Ferroelectrics* **76**, 241 (1987)
27. V.V. Shvartsman, D.C. Lupascu, *J. Am. Ceram. Soc.* **95**(1), 1 (2012)
28. K. Uchino, S. Nomura, *Ferroelectrics* **44**, 55 (1982)
29. W. Li, K. Chen, et. al, *Appl. Phys. Lett.* **85**, 4717 (2004)
30. K. Kumar, B. Kumar, *J. Ceram. Int.* **38**, 1157 (2012)
31. Ming-Ding et.al, *J. Mater.* (2018)
32. G. Singh, et al., *J. Appl. Phys.* **107**, 064103 (2012)
33. H. Liu, et. al, *Nat. Mater.* **11**, 422 (2012)
34. B. Tiwari, R.N.P. Choudhary, *J. Alloys Compd.* **493**, 1 (2009)
35. B. Tiwari, R.N.P. Choudhary, *IEEE Trans. Dielectr. Electr. Insul.* **17**, 5 (2010)
36. T.F. Zhang, et al., *AIP Adv.* **4**, 107141 (2014)
37. D.P. Almond et al., *Solid State Ionics* **8** (2), 159 (1983)
38. A.K. Jonscher, *J. Mater. Sci.* **13**, 553 (1978)
39. J.M. Le Meins, *Solid State Ionics* **111**, 67 (1998)
40. S.H. Chung et. al, *Phys. Rev. B* **41**, 6154 (1990)
41. A.K. Joncher, *J. Mater. Sci.* **16**, 2037 (1981)
42. R. Dridi et. al, *J. Alloys Compd.* **634**, 179 (2015)
43. A.A. Youssef Ahmed, *Z. Naturforsch.* **57**, 263 (2002)

Publisher's Note Springer Nature remains neutral with regard to jurisdictional claims in published maps and institutional affiliations.